Combinatorial Discovery and Optimization of a Complex Oxide with Water Photoelectrolysis Activity

Michael Woodhouse and B. A. Parkinson*

Department of Chemistry, Colorado State University, Fort Collins, Colorado 80523

Received October 29, 2007. Revised Manuscript Received December 30, 2007

A ternary oxide containing cobalt, aluminum, and iron and not previously known to be active for the photoelectrolysis of water was identified using a high throughput combinatorial technique. The technique involves ink jet printing overlapping patterns of oxide precursors onto fluorine-doped tin oxide conductive glass substrates. Subsequent pyrolysis yields patterns of mixed oxide compositions that were screened for photoelectrolysis activity by scanning a laser over the material while it was immersed in an electrolyte and mapping the photocurrent response. The composition and optimum thickness for photoelectrochemical response of the newly identified material was further refined using quantitative ink jet printing. Chemical analysis of bulk and thin film samples revealed that the material contains cobalt, aluminum, and iron in a Co_3O_4 spinel structure with Fe and Al substituted into Co sites with a nominal stoichiometry of $Co_{3-x-y}Al_xFe_yO_4$ where x and y are about 0.18 and 0.30, respectively. The material is a p-type semiconductor with an indirect band gap of around 1.5 eV, a value that is nearly ideal for an efficient single photoelectrode for water photoelectroylsis. Photoelectrochemical measurements indicate that the onset of hydrogen evolution is about 0.9 V positive of the thermodynamic value but the photocurrent is limited by slow kinetics for hydrogen evolution.

Introduction

Efficient and inexpensive production of hydrogen from water and sunlight has been the "holy grail" of photoelectrochemistry since Fujishima and Honda first demonstrated the feasibility of the process with rutile crystals.[1–4] Realistically however, single-crystal oxide materials will most likely not be efficient or cost-effective photoelectrolysis materials due to the expense of single crystal growth, the low absorption coefficients of metal $d-d$ transitions and the low mobility of charge carriers in metal d-bands. Nonetheless, nanostructured oxide semiconductors are promising materials for this purpose due to their inherent stability, increased absorption capabilities relative to bulk materials, and potential for low cost. A porous nanostructure of titanium dioxide has already proven to be worthwhile as a scaffold and electron collecting phase for dye-sensitized photovoltaic devices that could potentially be highly efficient and made at low-cost[5,6] and a nanotubular TiO_2 morphology has substantially increased the efficiency of water photoelectrolysis using ultraviolet wavelengths.[7,8]

The nanostructuring of a metal oxide for solar photoelectrolysis provides several advantages. First, as mentioned above, it can be produced at low cost. Second, as in a dye-sensitized solar cell, all photons are eventually absorbed and the photogenerated carriers are produced near an interface where the photoelectrolysis reactions occur and so high carrier mobilities are not essential. Third, the lower microscopic current density of a high-surface-area nanostructured material will reduce the overpotential needed to drive the oxidation and reduction of water at acceptable rates, resulting in higher conversion efficiencies. Lastly, a nanostructured oxide can be deposited on a transparent conducting substrate that allows for back illumination, as in the dye-sensitized solar cell, reducing the scattering of the incoming solar radiation by bubbles generated at the electrode surface.

The roadblock for the realization of such a system has been that no semiconducting material is known that simultaneously satisfies all of the criteria needed for efficient photoelectrolysis: the material must be stable for many years under illumination in aqueous electrolyte solution, have a band gap within the range where it can absorb a large fraction of the solar photons (1.5–2.0 eV for a single photoelectrode system), have conduction and valence band positions that straddle the oxidation and reduction potentials of water, and be catalytic for water reduction or oxidation.[9,10]

We believe that the material will most likely be an oxide semiconductor in order to be stable for many years in sunlight while immersed in an electrolyte. There are many oxide materials that have been evaluated for their ability to

* Corresponding author. E-mail: Bruce.Parkinson@colostate.edu.

(1) Fujishima, A.; Honda, K. *Nature* **1972**, *238*, 37–38.
(2) Fujishima, A.; Honda, K. *Bull. Chem. Soc. Jpn.* **1971**, *44*, 1148–1150.
(3) Fujishima, A.; Kohayakawa, K.; Honda, K. *J. Electrochem. Soc.* **1975**, *122*, 1487.
(4) Gratzel, M. *Nature* **2001**, *414*, 338.
(5) Nazeeruddin, M. K.; Kay, A.; Rodicio, I.; Humphry-Baker, R.; Muller, E.; Liska, P.; Vlachopoulous, N.; Gratzel, M. *J. Am. Chem. Soc.* **1993**, *115*, 6382–6390.
(6) Regan, B. O.; Gratzel, M. *Nature* **1991**, *353*, 737.
(7) Grimes, C. A. *J. Mater. Chem* **2007**, *17*, 1451–1457.
(8) Grimes C. A. Nanotechnology 2007 *18* 6.
(9) Tan, M. X.; Laibinis, P. E.; Nguyen, S. T.; Kesselman, J. M.; Stanton, C. E.; Lewis, N. S. *Prog. Inorg. Chem.* **1994**, *41*, 21–145.
(10) Rajeshwar, K. *J. Appl. Electrochem.* **2007**, *37*, 765–787.
(11) Jarrett, H. S.; Sleight, A. W.; Kung, H. H.; Gilson, J. L. *J. Appl. Phys.* **1980**, *51* (7), 3916–3925.

10.1021/cm703099j CCC: $40.75
Published on Web 03/08/2008

photoelectrolyze water.[10,11] α-Fe_2O_3 has recently,[12–14] and in the past,[15] received a lot of attention for its water photooxidation activity; however, its band gap (2.2 eV) is larger than the optimum for a single band gap device to efficiently use the solar spectrum for water photoelectrolysis.[16] We contend that a more suitable oxide material will contain multiple metals that will each contribute to the required properties of stability, light absorption, and being catalytic for hydrogen or oxygen evolution. Therefore, we developed a high throughput combinatorial approach to prepare and rapidly screen many multiple-metal containing oxides for photoelectrolysis activity.[17] Briefly, our method involves ink jet printing metal oxide precursors (to date, primarily nitrate salts) in overlapping patterns onto conducting glass substrates. Subsequent pyrolysis of the substrate yields multiple oxide phases that can be screened for photolectrolysis activity by measuring the photocurrent generated by scanning a laser over the material while it is immersed in an electrolyte. To date, we have printed and screened almost 500 combinations of four metals taken three at a time and have identified a number of previously unrecognized materials that have photoelectrolysis activity. In this paper, we discuss how we have developed a methodology to follow up on "hits" in the high throughput screening and attempt to understand and optimize a new material's water photoelectrolysis activity.

Experimental Section

Precut flourine-doped tin oxide coated glass (TEC 8, 8-ΩR, 3.0 mm thickness) was obtained from Pilkington Industries. $CsNO_3$, $Fe(NO_3)_3$, $Cu(NO_3)_2$, $Co(NO_3)_2$, and $Al(NO_3)_3$ were obtained from Sigma Aldrich (Fe, Cu, and Co) or Baker (Al) and were used as received. $TiCl_4$ packaged under argon was obtained from Alfa-Aesar and placed into an oxygen and moisture-free glovebox prior to opening. A 2 M aqueous solution (which is surprisingly stable under ambient conditions) of the titanium precursor was prepared by filling a syringe with the appropriate amount of $TiCl_4$ in the glovebox and carefully adding it dropwise to distilled water immersed in an ice bath with continuous stirring. This aqueous solution was diluted to the same concentration as the other precursors, 0.5 M, just prior to printing.

The triangular gradient ink jet patterns were produced as described previously using a Hewlett-Packard Deskjet 1220C thermal ink jet printer.[17] The combinatorial template with quantitative stoichiometries was printed with a Fujifilm Dimatix model DMP-2800 piezoelectric ink jet printer. A formulation suitable for the Dimatix inkjet printer used solutions of the appropriate metal nitrate salts (0.50 M) with 35%, by volume, diethylene glycol and 1%, by volume, diethylene glycol monobutyl ether to serve the respective roles of viscosity agent and surfactant. The solutions were sonicated for 10 min to ensure complete dissolution and were then injected through a 2 μm syringe filter into empty 10 pL drop volume Fujifilm Dimatix printer cartridges. Prior to printing, a cleaning cycle was run on each cartridge to ensure that printing was uniform as verified by a print head camera that is built into the Fujifilm Dimatix printer. The printer also allows an accurate determination of drop volumes, the number of nozzles firing, the piezoelectric jetting waveform for individual nozzles, and the frequency of nozzle firing, all important for a quantitative determination of the amount of each component printed within the combinatorial template. Prior to printing the glass was soaked in a piranha solution followed by rinsing with copious amounts of distilled water. The SnO_2:F glass was then taped to the printer platen that was heated to 50 °C. Methanol was rubbed onto the substrate to make it slightly hydrophobic in order to minimize spreading of the "inks" and to maintain separation between the printed squares. The metal precursor solutions were often over printed up to three times in order to achieve the appropriate metal oxide thickness.

The printed metal precursor patterns were then pyrolyzed in air for approximately 2 h at 500 °C in a ThermoLyne type 1300 furnace to convert the precursors into metal oxides. For initial screening of the metal oxide candidates, the printed films were connected to a Princeton Applied Research 174A Potentiostat as the working electrode with a platinum basket functioning as both the counter and reference electrodes in a two-electrode configuration. A 0.10 M NaOH solution was typically used as the electrolyte. The sample was irradiated with a 532 nm frequency doubled Nd:YAG laser (model LAGR20 from Information Unlimited) with a beam diameter of ca. 1 mm and a typical illumination intensity of approximately 2500 mW/ cm^2. The laser beam was modulated with a PTI OC-4000 chopper operating at 31 Hz and was rastered over the film by applying stepwise voltages to a two-mirror galvanometer (CLS-200 from Intelite, Inc.). The resulting photocurrent at each pixel (generally around 10 $\mu A/cm^2$ at short-circuit, zero bias for the working materials) was measured after 300 ms illumination times with a Stanford Research Systems SR530 model lock-in amplifier and this data was used to generate the false color photocurrent images.

Glancing angle X-ray diffraction (GAXRD) measurements were performed with a Bruker D-8 Discover instrument using Cu K-α radiation. GAXRD measurements were performed in the 2θ range from 5 to 80 degrees, at an angle of incidence of 0.5 degree, a step size of 0.02°, and time-per-step of 10 s. Search match analysis for identification of crystalline phases was performed using Bruker EVA software. Bulk samples for powder X-ray diffraction were prepared by mixing the appropriate amounts of nitrate salts to a total concentration of 0.5 M in distilled water with 35% by volume diethylene glycol and 1% by volume diethylene glycol monobutyl ether and pyrolyzing at 500 °C. Powder X-ray diffraction measurements were performed by using a Scintag-X2 diffractometer equipped with a Peltier detector and Cu X-ray tube. XRD scans were performed over the 2Theta range from 5 to 80 degrees with a step of 0.02 degree and time-per-step of 1 s. Photocurrent spectroscopy was done using an apparatus that has been described previously[18] while SEM and EDS images were taken with a field-emission JEOL 6500F electron microscope.

Larger area photoelectrodes were made by printing from a cartridge containing a solution of precursors mixed at the optimized bulk catalyst composition onto mica substrates coated with evaporated layers of Au (250 nm) with a 50 nm Cr adhesion layer. Current–voltage analysis was performed with a computer-controlled CompactStat potentiostat made by Ivium Technologies using a saturated sodium calomel electrode (SSCE) as the reference electrode and a platinum basket as the counter electrode. The sweep

(12) Cesar, I.; Kay, A.; Martinez, J. A. G.; Gratzel, M. *J. Am. Chem. Soc.* **2006**, *128*, 4582–4583.
(13) Duret, A.; Gratzel, M. *J. Phys. Chem. B* **2005**, *109*, 17184–17191.
(14) Kay, A.; Cesar, I.; Gratzel, M. *J. Am. Chem. Soc.* **2006**, *128*, 15714–15721.
(15) Leygraf, C.; Henderwerk, M.; Somorjai, G. A. *J. Phys. Chem.* **1982**, *86*, 4484–4485.
(16) Heller, A. Hydrogen Evolving Solar Cells. *Science* **1984**, *223*, 1141–1148.
(17) Woodhouse, M.; Herman, G.; Parkinson, B. A. *Chem. Mater.* **2005**, *17*, 4318.
(18) Takeda, N.; Parkinson, B. A. *J. Am. Chem. Soc.* **2003**, *125*, 5559–5571.

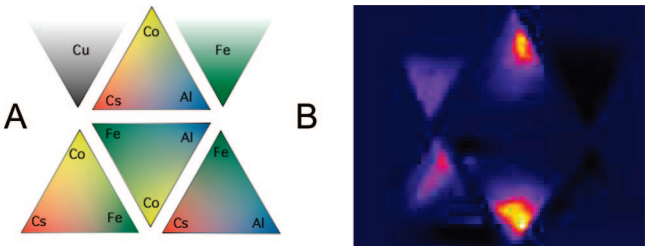

Figure 1. (A) Template showing the gradient pattern used for printing the metal nitrate precursors for the Al−Co−Cs−Fe system (Fe and Cu triangles are internal standards for n- and p-type photoactivity, respectively). (B) Laser screening at 532 nm with no applied bias in a 0.1 M NaOH solution. Qualitatively, it can be seen that the highest activity is associated with primarily Co and small amounts of Fe and Al. The printed triangles have a height of 1.9 cm.

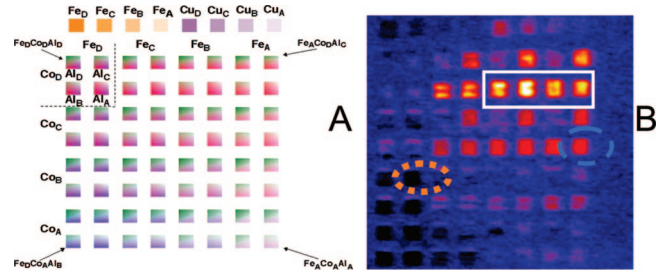

Figure 2. (A) Printing template used for quantifying the optimal stoichiometry in the Co−Al−Fe system where known amounts of the components are printed into individual 3 mm × 3 mm squares. The density of precursor drops (and the resulting stoichiometry) is shown in Table 1. (B) False color photocurrent map with no applied bias at 532 nm in a 0.1 M NaOH solution. The cathodic photocurrent measured by laser scanning the brightest square of the film is nearly three times that generated by the best pure CuO internal standard labeled Cu_D. The compositions within the solid white box were expanded in Figure 3.The materials within the dashed blue and dotted orange circles were used for the action spectra shown in Figure 4.

rate was 0.5 mV/ s for the electrodes immersed in a 0.1 M NaOH solution deoxygenated with nitrogen. The sample was irradiated with a 150 W Xe arc lamp for the photocurrent–voltage curves. The lamp was placed approximately 25 cm from the sample as this was the optimum working distance for focusing the unfiltered light onto the 2.5 cm × 2.5 cm printed sample. Platinization was accomplished by sweeping the potential of the illuminated electrode at 5 mV/s for three cycles between +0.1 and −0.3 V vs SSCE in a deoxygenated pH 4 acetic acid/sodium acetate buffer containing 100 μM H_2PtCl_6.

Results and Discussion

We have used a consumer level ink jet printer to print and screen hundreds of different material combinations using the four metals taken three at a time pattern used to screen fuel cell catalysts.[19] Most of the material combinations show no or very little photoresponse while a few have performed significantly better than the internal reference materials (α-Fe_2O_3 and CuO for n- and p-type photoactivity, respectively[20]). One of the materials discovered in our search has reproducibly shown substantial p-type photactivity. Figure 1 shows the photocurrent map done in 0.1 M NaOH without an externally applied bias of a "four metals, three at a time" printed and fired film using Fe, Co, Al, and Cs. The dark regions represent areas where the photocurrent is in the anodic direction whereas the bright regions show areas of p-type photocurrent response that are 2−2.5 times larger than the CuO internal standard (upper left triangle). The regions of high activity are found in the Co rich regions of the Co−Al−Fe and Co−Al−Cs triangles. Although we can tell from the gradient printing that the active phase is cobalt-rich, the exact proportions of the metal components in the active mixture are unknown since we do not know the exact amounts of the various inks delivered by the printer driver software as its usual function has been optimized for visual aesthetics when printing conventional inks.

To more quantitatively refine the composition of the photoactive phase, we focused on the Co−Fe−Al containing semiconducting oxide and employed a research grade inkjet printer that allows quantification of the ink-jetted volumes and dot densities. A printing template was created, similar to patterns used for combinatorial phosphor discovery,[21,22] where an array of squares is printed that each contain a predetermined amount of the three oxide precursors as shown in Figure 2A. The total amount of precursor deposited into each square is determined from the concentration of metal nitrate in the printing solution, the drop volume for a printed drop, the number of layers printed, and the number of drops ink jetted per unit area, an amount that is determined by the density of dots and the number of ink-jetting nozzles firing from each cartridge. A series of the internal standards, α-Fe_2O_3 and CuO, of different dot densities (thicknesses) are also printed at the top of the pattern. In this pattern, four different densities of Co and Fe were printed as double horizontal and double vertical rows, respectively. Different amounts of Al were deposited in a repeating pattern within groups of four squares containing identical Fe and Co amounts as shown in the dashed inset in the upper left-hand corner of Figure 2A.

Table 1. Density of Printed Precursor Drops Used to Produce the Mixtures Shown in Figure 2

label	1D drop spacing (μm)	drops per mm^2	relative stoichiometry
A	160	45	1
B	120	75	1.7
C	80	169	3.7
D	40	642	14.4

Controlling the density of the printed drops allows the production of a broad or narrow compositional range containing known stoichiometries within each square when the other factors mentioned above are held constant. Table 1 contains the values of drop spacing and density used in Figure 2 for the Fe and Cu internal standards and the Fe−Co−Al Oxide precursors. For illustrative purposes, the bottom square on the far left, labeled $Fe_DCo_AAl_B$, was printed with a drop spacing of 40 μm, 160 μm, and 120 μm for Fe, Co, and Al, respectively. The drop density is then calculated by dividing the area of the square (9 mm^2) into the

(19) Reddington, E.; Sapienza, A.; Gurau, B.; Viswanathan, R.; Sarangapeni, S.; Smotkin, E. S.; Mallouk, T. E. *Science* **1998**, *280* (5370), 1735.
(20) Koffyberg, F. P.; Benko, F. A. *J. Appl. Phys.* **1982**, *53* (2), 1173–1177.
(21) Danielson, E.; Devenney, M.; Giaquinta, D. M.; Golden, J. H.; Haushalter, R. C.; McFarland, E. W.; Poojary, D. M.; Reaves, C. M.; Weinberg, W. H.; Wu, X. D. *Science* **1998**, *279*, 837–839.
(22) Wang, J.; Yoo, Y.; Gao, C.; Takeuchi, I.; Sun, X.; Chang, H.; Xiang, X.-D.; Schultz, P. G. *Science* **1998**, *279*, 1712–1714.

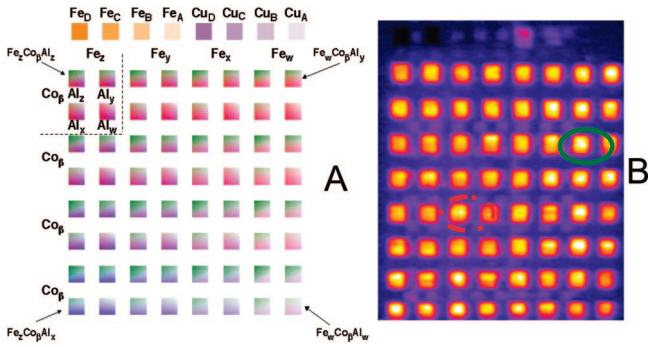

Figure 3. Compositional library produced by expansion of the compositional region outlined by the white box in Figure 2. The template shown in (A) was created by including all of the mixtures created within the inset of Figure 1 as well as some intermediate stoichiometries. The actual densities are shown in Table 2, whereas the pure Fe and Cu internal standards are printed as in Figure 2. (B) Photocurrent map of the array of 3 mm × 3 mm squares measured in 0.1 M NaOH with a 532 nm laser. The compositions within the solid green and dashed−dotted dotted red circles were used for the action spectra shown in Figure 4.

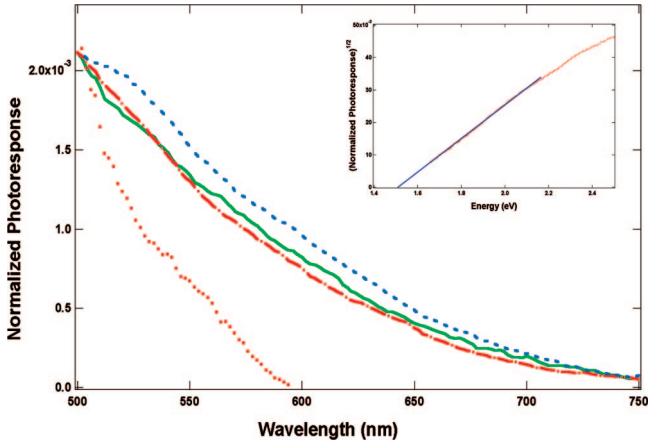

Figure 4. Action spectra normalized to a constant value at 500 nm for the dotted orange data and dashed blue data obtained from the compositions outlined in Figure 2 and the solid green and dashed−dotted red data obtained from the compositions outlined in Figure 3. The direction of the photocurrent was also inverted for the iron-rich composition (outlined by the orange dotted circle in Figure 2). The inset shows a linear extrapolation to approximate the band gap of the p-type materials from the average IPCE values fit to an indirect transition.

corresponding number of drops of each material printed within that square with small corrections when the width of the square is not an integer value of the drop spacing. As the relative stoichiometry of each material would be directly proportional to the relative density of material deposited, this square corresponds to a nominal stoichiometry of $Fe_{14.4}Co_1Al_{1.7}$. As another example, the brightest square in Figure 2B, third square from the right, third row down, is given the label $Fe_B\ Co_DAl_A$ which correlates to $Fe_{1.7}Co_{14.4}Al_1$ (In atomic percentages 10% Fe, 84% Co, and 6% Al) and this composition was used in future experiments where bulk samples were prepared.

To further refine the optimal composition of the photocatalyst, another template was created that encompasses stoichiometries outlined by the white box in Figure 2B as well as some similar stoichiometries. The template, and the result of the photocurrent screening, is shown in Figure 3. In this pattern the amount of cobalt was kept constant (labeled β in the figure with a drop spacing equal to that of all mixtures within the white box of Figure 2B), whereas the Fe and Al contents (labeled w, x, y, and z) were varied and calculated using the rationale described previously. The internal standards were printed with the same drop densities described in Table 1 as A, B, C, D (note that the overall amount of printed internal standard material relative to the working mixtures is approximately the same between Figures 2 and 3 in order to not overestimate the contribution of sample thickness to performance). The resulting photocurrent is within ±20% for all squares, indicating flexibility in the stoichiometries of photoactive compositions. Indeed, the Fe and Al content can vary by as much as a factor of 2 (between $Co_{17.8}Fe_1Al_{2.1}$ and $Co_{17.8}Fe_{2.1}Al_1$) and still produce a material with comparable photoactivity.

Table 2. Density of Printed Precursor Drops Used to Produce the Mixtures Shown in Figure 3

label	1D drop spacing (μm)	drops per mm^2	relative stoichiometry
w	180	36	1
x	160	45	1.25
y	140	54	1.5
z	120	75	2.1
β	40	642	17.8

The band gaps of the photoactive materials can be determined by measuring the photocurrent spectrum of the individual printed areas. Figure 4B shows *normalized* photocurrent spectra for several compositions identified in Figure 4A and illustrates that the iron-rich compositions have a photocurrent onset of about 2.2 eV, consistent with α-Fe_2O_3 being the active phase in these regions (note the photocurrent in this case was anodic). The gradual onset of the photocathodic current with increasing photon energy for the Co−Al−Fe phase indicates that the band gap is indirect and this is confirmed by plotting $(IPCE)^{0.5}$ against photon energy where a linear dependence with an intercept of about 1.5 eV is obtained (inset of Figure 4). Because the printed film is so thin, we assume that the photocurrent, and subsequently the IPCE, is directly proportional to the absorption coefficient (α) for the material and that carrier diffusion length plays no role in the photocurrent. The band gap of the new p-type phase appears to be essentially independent of composition over the range $Co_{3.7}Al_1Fe_1$–$Co_{17.8}Al_{2.1}Fe_1$. There are several interpretations for this observation. Either there is a very stable stoichiometry that forms even when there is an excess of one or two of the components present and variations in the photoresponse are the result of variations in the doping level of this phase or the band gap is not a strong function of the Fe or Al content of the phase in this composition region.

Once the near optimum initial composition was determined (~84% Co, 10% Fe, and 6% Al), a bulk solution containing a total metal ion concentration of 0.5 M, including the appropriate amount of viscosity agent and surfactant, was prepared for printing. The combined solution was then printed onto a SnO_2:F substrate and fired in a furnace at 500 °C for 2 h. A larger volume was also pyrolzed at the same temperature to prepare a bulk powder sample. The printed film was examined with glancing angle X-ray diffraction and the bulk sample with powder X-ray diffraction. Diffracto-

grams from both methods show the same lines with additional lines from the tin oxide substrate appearing in the thin film sample. Indexing the X-ray pattern reveals that the material has the same X-ray pattern as Co_2AlO_4,[23] $CoAl_2O_4$,[24] and Co_3O_4.[25] Surprisingly there are only very small shifts (0.1–0.2°) in the major diffraction peaks for all of these compounds where Al^{3+} substitutes for Co^{3+} in Co_3O_4 through the entire composition range to $CoAl_2O_4$.[26,27] Because the shifts are so small, X-ray diffraction does not provide a good estimate of the amount of Al substitution into our cobalt rich active phase. Iron substituting into the Co_3O_4 phase for either Co^{3+} or Co^{2+}, due to its similar ionic radius, would also not shift the diffraction peaks very much. Due to iron having one less electron than cobalt, it may be acting as a dopant and imparting the p-type behavior. Noticeably absent in the diffractogram are peaks assignable to either α-Fe_2O_3 or Al_2O_3, suggesting that iron may replace some cobalt in the lattice or the presence of amorphous oxide phases for the remaining constituents within the sample.

Recent theoretical work performed by Walsh et al.[28] on a number Co−Al−Fe spinel stoichiometries predicts that the electronic band gap of Co_3O_4 remains largely unchanged as Al is substituted for cobalt into the lattice to form Co_2AlO_4 but does increase noticeably for $CoAl_2O_4$ as all the octahedral metal sites are replaced with Al. Additionally, $CoAl_2O_4$ has been identified as a likely direct gap binary oxide candidate with properties suitable for photoelectrolysis if its otherwise large band gap is reduced by, for example, doping, local cation disorder, or crystal defects. The potential role of Fe to induce such changes appears to corroborated by experiments where samples prepared with only Co−Al binary oxide compositions showed lower photoactivity than the optimal stoichiometry by more than a factor of 2.

To further optimize the performance of the Co−Fe−Al oxide system, we prepared cartridges containing the nitrate salts near the optimal composition ratio with a total concentration of 0.50 M. The single cartridge could then be used to print different spot densities or to print multiple layers in order to vary the thickness of the resulting multicomponent oxide film. Figure 6 shows the results of such a study. Assuming that the density of the final material is close to that of Co_3O_4, we can estimate the sample thickness shown in Figure 3.

The area labeled 1 is the thickest film and shows very little photocurrent except for the thinner areas around the periphery. The printed area labeled 2 is the best thickness produced in this experiment since it has the highest photocurrent yield. The thickness of the film is further decreased from areas 3 and 4 in the figure and the photocurrent also decreases.

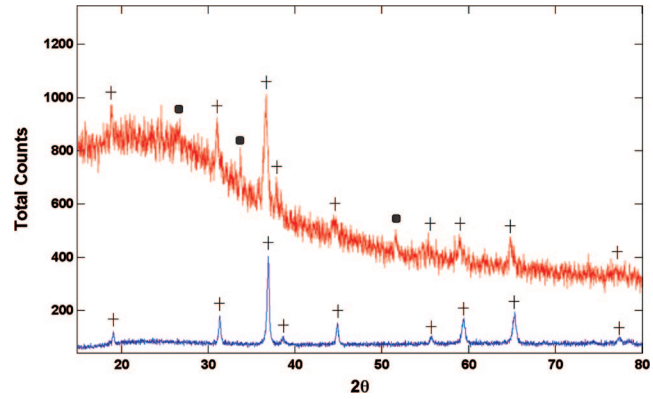

Figure 5. Glancing angle XRD (top curve in red) for a film printed onto a flourine-doped tin oxide substrate and powder XRD for the 84% Co, 10% Fe, and 6% Al bulk sample (bottom in blue). The 2θ axis was truncated in order to display the flatter regions of the GAXRD curves and because no features were present below that range. The filled circles are the major peaks corresponding to tin oxide, whereas the crosses correspond to the major peaks for Co_3O_4 and/or Co_2AlO_4 to $CoAl_2O_4$.

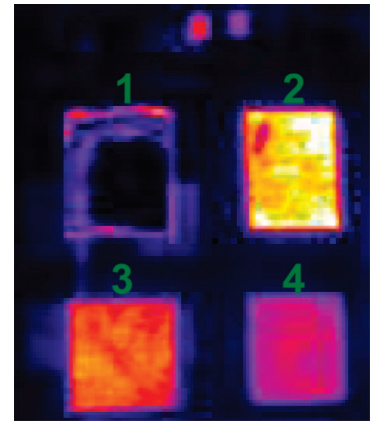

Figure 6. Thickness optimization for the optimized stoichiometry printed onto a flourine-doped tin oxide substrate. The four larger squares were printed with the differing dot densities (shown in Table 3) inside of 1.5 cm × 1.5 cm squares. Each was printed from a single cartridge containing, in atomic percentages, 84% Co, 10% Fe, and 6% Al. The iron and copper internal standards (smaller squares at the top of the image) were printed as in Figures 2 and 3. The photocurrent mapping was done in 0.1 M NaOH at 532 nm. See the text for a more complete description.

Table 3. Drop Spacing and Calculated Average Thickness for the Four Squares Printed and Mapped for Photoactivity in Figure 6

label	1D drop spacing (μm)	drops per mm^2	calcd average thickness (nm)
1	10	10.013	560
2	30	1.115	60
3	50	403	24
4	70	205	12

Another advantage of printing optimized films from a single cartridge is that it provides a method for adding a fourth component to the material. Figure 7 shows an example of adding a fourth metal to our optimized composition. Of course, we are only sampling a line within a complex four-dimensional phase diagram but such a study may still reveal even more directions for optimizing composition. In Figure 5, a small alkali metal cation (Li), a large alkali cation (Cs), some metal ions with ionic radii near that of Co and Fe (Mg, Zn), and Ti were added to the optimal composition. The upper row of five squares is the optimized ternary Co−Fe−Al phase and the fourth component has decreasing concentra-

(23) JCPDS-ICDD Card 38–814; p JCPDS-ICDD Card No. 44–160; International Centre for Diffraction Data: Newton Square, PA.
(24) JCPDS-ICDD Card 44–160; p JCPDS-ICDD Card No. 44–160; International Centre for Diffraction Data: Newton Square, PA.
(25) JCPDS-ICDD Card 42–1467; p JCPDS-ICDD Card No. 44–160; International Centre for Diffraction Data: Newton Square, PA.
(26) Stangar, U. L.; Orel, B.; Krajnc, M. *J. Sol−Gel Sci. Technol.* **2003**, *26*, 771–775.
(27) Zayat, M.; Levy, D. *Chem. Mater.* **2000**, *12*, 2763–2769.
(28) Walsh, A.; Wei, S.-H.; Yan, Y.; Al-Jassim, M.; Turner, J. A.; Woodhouse, M.; Parkinson, B. A. *Phys. Rev. B* **2007**, *76*, 165119.

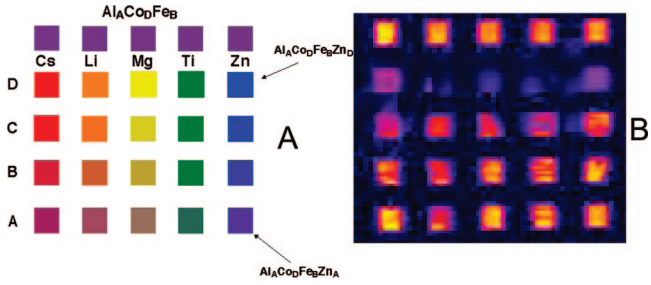

Figure 7. Adding a fourth component to the optimized ternary composition into individual 4 mm × 4 mm squares. (A) Template used for mixing Cs, Li, Mg, Ti, and Zn with the optimized Al, Co, and Fe stoichiometry discussed earlier. The letters correspond to the same drop densities as in Figure 2. (B) Photocurrent map of the compositions in 0.1 M NaOH using a 532 nm laser.

tions in the lower squares. It is clear that in this case the fourth component decreases the photoresponse in all cases except for the smallest added amounts that have very little effect on the photoresponse. This technique could also be used for adding a catalyst layer by firing the optimal composition before printing a layer of catalyst for water oxidation or reduction that can itself be optimized for thickness and composition.

Larger area films near optimal composition and thickness were then printed to measure their current–voltage behavior. Although deposition of the material onto the usual fluorine-doped tin oxide substrate would have been consistent and convenient, there were problems with this substrate when polarized in electrolytes at cathodic potentials. We eventually determined that the reduction and reoxidation of the tin oxide underlayer during potential cycling in the electrolyte led to delamination of the printed film from the transparent conductive oxide surface, perhaps due to lattice strain at the interface. After trying a number of other substrates, evaporated gold on mica, with a thin chromium adhesion layer, showed the best behavior for printed film adhesion, low dark currents and electrochemical stability. Evaporated Au on mica films are known to give a flat, polycrystalline but predominately (111) orientated film.[29] The morphology of the pyrolyzed film was significantly different on Au than it is on FTO as can be seen in the SEM images on the two substrates in Figure 8. The film printed and fired on the Au substrate is discontinuous and, based upon the drop spacing set within the printer software as compared to the spacing of the catalyst islands seen in the SEM, it appears that a number of printed drops coalesce during annealing and do not wet the gold substrate. We estimate that less than 50% of the area of the gold layer is covered by the photocatalyst. EDS analysis of the dark and light regions of figure 6B confirm that the catalyst is confined to the dark islands and that the expected metal stoichiometry is measured within the islands. The film appears to be more continuous when printed on FTO but has a more porous appearance at higher magnifications.

The films printed onto Au on mica were stable for multiple voltammetric cycles in basic electrolytes and so the dark and photocurrent response for hydrogen evolution was investigated in deoxygenated 0.1 M NaOH solution. Less than 40 μA/cm^2 of dark current was generated near the onset for dark hydrogen production (−0.98 V vs SSCE). When the printed area containing the photocatalyst is illuminated a photocurrent onset at about −0.10 V is observed with a plateau region followed by an increase in the photocurrent as the thermodynamic potential for the onset of dark hydrogen production is reached. The photocurrent onset indicates an onset of hydrogen evolution about 0.9 V positive of the thermodynamic potential in 0.1 M NaOH, very respectable for a material with a band gap of 1.5 eV. The photocurrent near the thermodynamic potential of the hydrogen electrode is about 170 μA/cm^2 and remained steady (within ±0.5%) for illumination times of over thirty minutes. Calculation of the total amount of charge collected due to photocurrent at short circuit is about an order of magnitude greater than needed for the complete reduction of the deposited oxides to their metallic form indicating that the material is catalytic for photoreduction of water since water is the only reducible species present in the electrolyte.

The poor fill factor in the power curve for hydrogen production could be due to poor electrode kinetics for the hydrogen evolution reaction. Previously photocathodes with little catalytic activity for hydrogen evolution could be significantly improved by the deposition of Pt nanoparticles onto their surface.[16,30,31] In an attempt to produce more photocurrent for hydrogen production, the sample was immersed into a platinizing solution and islands of Pt metal were deposited by illuminating the electrode during three cyclic voltammetry cycles from 0.1 to −0.3 V. Upon the sample being reimmersed into the NaOH solution, the photocurrent was observed to increase as the platinum deposition reduced the overpotential needed for hydrogen production both in the light and in the dark, as can be seen by the earlier onset of bulk hydrogen production. The increase and plateau of the photocurrent in the potential region between −0.2 and −0.6 V may be due to the presence of catalytic sites for hydrogen evolution but the smaller photocurrent compared to the response at −0.9 V indicates that the Pt catalyst is not optimally configured to supply a catalytic path for all photogenerated carriers. Photocurrents at both of these potentials are dependent on the light intensity and so the rate of the catalytic reaction through the catalytic sites is not rate limiting. Further work is needed to optimize the size and distribution of Pt on the surface to improve the photogenerated hydrogen evolution.

The incident photon to current efficiency on the printed films is very low (on the order of 1×10^{-6} to 1×10^{-5} when using a high-power 532 nm laser in a short-circuit two electrode configuration), because in addition to the poor hydrogen generation kinetics, we purposely print very thin layers of material where most of the incident photon flux passes through the film and is not absorbed or, in the case of the films printed on Au, is reflected from the regions where

(29) Higo, M.; Fujita, K.; Tanaka, Y.; Mitsushio, M.; Yoshidome, T. *Appl. Surf. Sci.* **2006**, *252* (14), 5083–5099.

(30) Heller, A.; Aharon-Shalom, E.; Bonner, W. A.; Miller, B. *J. Am. Chem. Soc.* **1982**, *104*, 6942.

(31) Deutsch, T.; Koval, C. A.; Turner, J. A. *J. Phys. Chem. B* **2006**, *110*, 25297–25307.

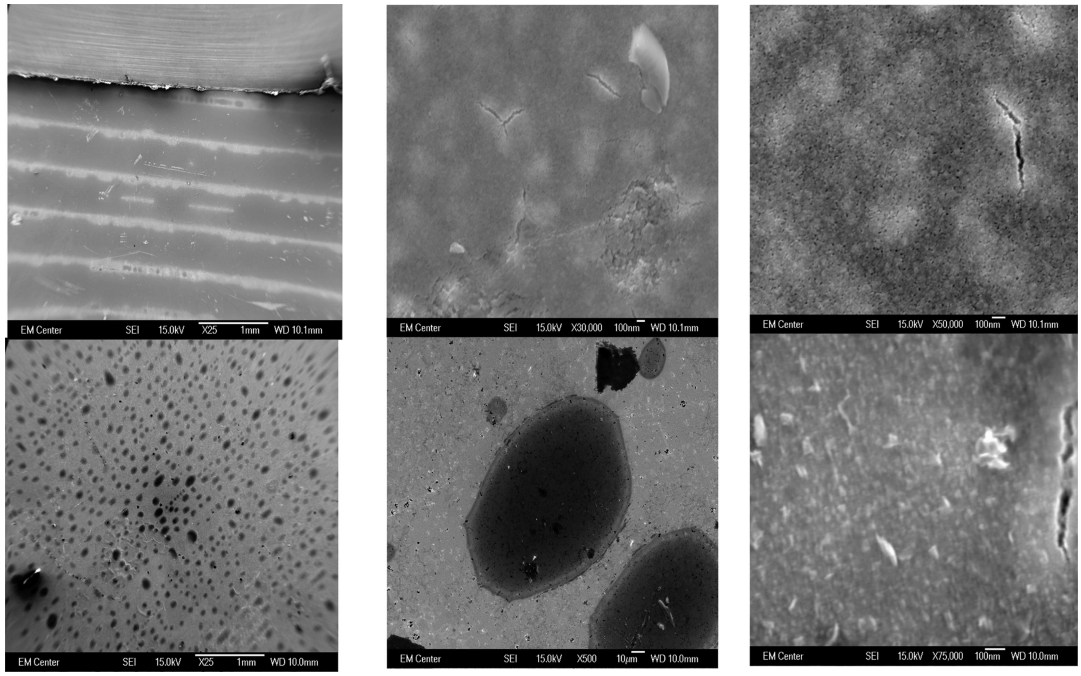

Figure 8. SEM images at different magnifications for the film used for measurement of the current–voltage curves (below) and sample printed on FTO (above). Substrate wetting and morphology are clearly different for the two substrates. EDS results confirm the designed and printed atomic percentages of Co, Fe, and Al within the dark islands of the bottom images.

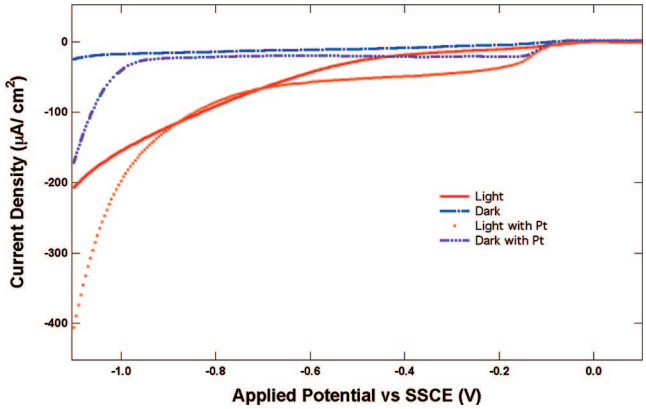

Figure 9. Dark and photocurrent–voltage curves for a 2 cm × 2 cm film printed onto a gold-on-chromium-on-mica substrate immersed in deoxygenated 0.1 M NaOH. The sweep rate was 0.5 mV/s. Illumination is from a 150 W Xe lamp. Platinization was done by immersing the electrode in a pH 4 acetic acid/sodium acetate buffer containing 100 M $H_2PtCl_6$and cycling three times between +0.1 and –0.3 V vs SSCE at a sweep rate of 5 mV/s.

there is no film (images c and d in Figure 8). Thin nanostructured films reduce the influence of carrier transport on the measured photocurrent. Carrier mobilities in transition metal oxides are quite low and, when coupled to the low absorption coefficients associated with forbidden d−d optical transitions, would result in low carrier collection in even a single crystal of a semiconducting photoelectrode. Therefore a thick high surface area nanocrystalline film, reminiscent of the dye sensitized solar cell, will most likely be the most efficient and cost-effective way to configure a photoelectrolysis device based on transition metal oxides. In this configuration the film will be thick enough to absorb all of the light and the size of the particles will be near or smaller than the carrier diffusion length resulting in all of the photogenerated carriers making it to the electrolyte interface to carry out the photoelectrolysis reactions. Therefore the optimization of the configuration of a combinatorially discovered photoelectrolysis system is the second, and equally challenging, step in building a practical system. However, as previously discussed, the purpose of this paper is not to configure the newly discovered photocatalysts for optimum efficiency but rather to investigate the path from discovery of an oxide semiconductor to understanding both the optimal composition, photoelectrochemistry, stability, and the solid-state chemistry of the newly discovered materials.

Conclusion

We have developed a methodology to discover new materials useful for the photoelectrolysis of water. In this paper, we concentrated on determining the optimum composition and solid-state structure of one newly identified potential photocatalyst. The material contains cobalt, aluminum and iron in a Co_3O_4 spinel structure with Fe and Al substituted into Co sites with a nominal stoichiometry of $Co_{3-x-y}Al_xFe_yO_4$ where x and y are about 0.18 and 0.30, respectively. It is a p-type semiconductor with an indirect band gap of around 1.5 eV, a value that is nearly ideal for the efficient single photoelectrode photoelectroylsis of water. This new cobalt iron aluminum oxide is most likely not the "holy grail" of photoelectrochemistry that we seek. Nonetheless, concentrating efforts on newly discovered lower band gap oxides appears to be a fruitful endeavor and our methodology gives a rational approach for future discovery and optimization of such materials. Our results have highlighted the difficulty of developing a new material from its discovery to its deployment in an optimized, efficient and useful device. Not only will the composition and nanostructure need to be optimized but, in addition, inexpensive, stable,

and perhaps transparent substrates that are compatible with the material's morphology and chemical makeup must also be found.

Acknowledgment. This work was supported by the Office of Basic Energy Sciences of the United States Department of Energy under Grant DE-FG02-05ER15750. We thank Dr. Sandeep Kohli for assistance with the x-ray diffraction experiments. Helpful discussions and theoretical work done by John Turner, Yanfa Yan, Aron Walsh, Su-Huai Wei, and M. M. Al-Jassim at NREL are acknowledged, as is a discussion about the printed titanium precursor solution with Jordan Katz at the California Institute of Technology. Additionally, we are grateful to Greg Herman and David Punsalan with the Hewlett-Packard Corporation for continued discussions.

CM703099J